Impact of Strong Quantum Confinement on the Performance of a Highly Asymmetric Device Structure: Monte Carlo Particle-Based Simulation of a Focused-Ion-Beam MOSFET

Irena Knezevic, *Student Member, IEEE*, Dragica Z. Vasileska, *Member, IEEE*, and David K. Ferry, *Fellow, IEEE*

***Abstract*—A highly asymmetric 250 nm n-channel MOSFET, with a 70-nm p^+-implant placed at the source end of the channel (achievable by focused-ion-beam (FIB) implantation, so the device is named FIBMOS), has been simulated using a two-dimensional (2-D) coupled Monte Carlo–Poisson solver, in which quantum confinement effects have been taken into account by incorporating an effective potential scheme into the particle simulator. Although the device is a long-channel one, its performance is dictated by the highly doped p^+-implant at the source end of the channel, and it is crucial to properly account for the quantum-confinement effects in transport, especially at the implant/oxide interface. We show that parameters such as threshold voltage and device transconductance are extremely sensitive to the proper treatment of quantization effects. On the other hand, the built-in electric field, due to the pronounced asymmetry caused by the presence of the p^+-implant, drastically influences the carrier transport, and consequently, the device output characteristics, in particular the magnitude of the velocity overshoot effect and the low-field electron mobility.**

***Index Terms*—Asymmetric device structures, FIBMOS device, Monte Carlo simulation, quantization.**

I. Introduction

IN THE design of ultra-small devices, one has to deal with two contradictory requirements: 1) the reduction of short-channel effects, which necessitates the use of high substrate doping densities and 2) hot-carrier reliability increase and substrate current reduction, which require a reduction of the in-plane electric fields and therefore, smaller substrate doping density. A device structure that satisfies both requirements must have asymmetric doping profiles, and there has been a vast amount of theoretical and experimental effort to predict optimal device structures that can operate reliably at higher drain voltages and do not exhibit pronounced short-channel effects. Some representative devices proposed are summarized in Fig. 1 and include lightly-doped drain (LDD) devices, gate overlapped LDD structure (GOLD), halo source GOLD drain (HS-GOLD) [1] and graded-channel MOS (GCMOS) devices [2]. The last device structure overcomes the incompatible requirements of short-channel effects and hot-carrier reliability. As such, it is a rather promising way, in terms of reliability and performance, for downward scaling without the need to further reduce the power supply. Further improvements in this device structure have been made with the use of focused-ion-beam (FIB) implantation [3], which provides point-by-point control of the lateral dopant density at the source end of the channel, resulting in the so-called FIBMOS device structure (see Fig. 2). Device simulations, which employ hydrodynamic transport models [4]–[6] and direct solution of the Boltzmann transport equation (BTE) using the Monte Carlo particle-based simulations [7]–[9] have been employed to examine the benefits of the FIBMOS structure with respect to conventional MOSFET devices.

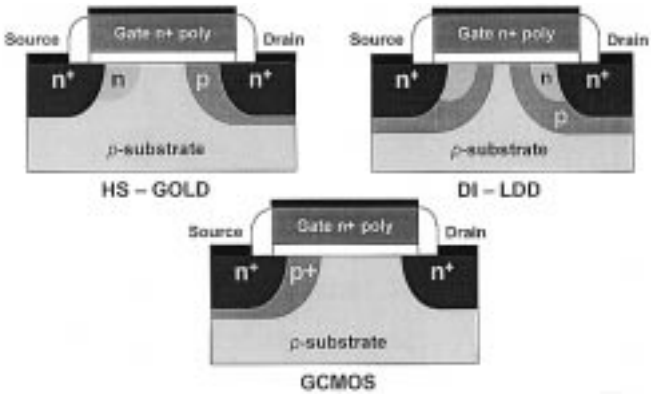

Fig. 1. Halo source GOLD drain (HS-GOLD), dual implant lightly doped drain (DI-LDD) devices, and graded-channel MOS (GCMOS) devices.

In this paper, we examine the influence of the quantum-mechanical space-quantization effects in the implant region of the FIBMOS on the device on-state performance. For this purpose, into a classical Monte Carlo particle-based simulator we incorporated an *effective potential* [10], a simple and very efficient approach to approximating quantum effects due to the nonzero size of an electron wave packet. Using a particle-based simulator is very important for such a pronouncedly asymmetric device (Fig. 2), as it is the only way to capture the velocity overshoot, which is present due to the high built-in electric fields. We present the simulation results for the electron sheet density,

Manuscript received December 17, 2001; revised February 11, 2002. This work was supported in part by the Semiconductor Research Corporation, the Office of Naval Research, under Contract N000149910318 and the National Science Foundation under NSF-CAREER ECS-9875051. The review of this paper was arranged by Editor C.-Y. Lu.

The authors are with the Department of Electrical Engineering and Center for Solid State Electronics Research, Arizona State University, Tempe, AZ 85287-5706 USA (e-mail: irenak@asu.edu; vasileska@asu.edu; ferry@asu.edu).

Publisher Item Identifier S 0018-9383(02)04886-4.

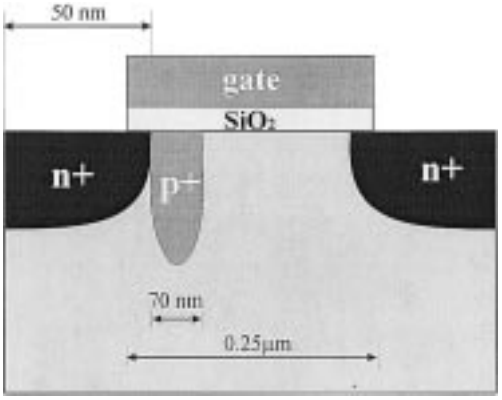

Fig. 2. Schematic representation of a FIBMOS device showing the extension of the source and drain regions and the FIB implant.

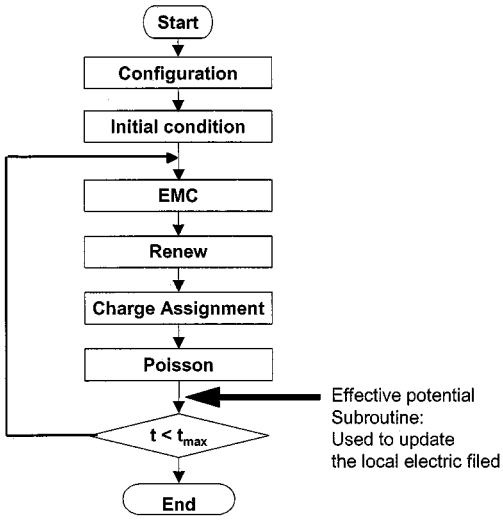

Fig. 3. Generic flow-chart of a Monte Carlo particle-based simulator with the effective-potential routine for including quantum-mechanical space-quantization effects.

average displacement of the carriers, device transfer and output characteristics, and the carrier mobility. We discuss the interplay of asymmetry and quantization and its impact on the device-performance estimates. We conclude this work with a summary and future direction of research.

II. Monte Carlo Particle-Based Simulator

The Monte Carlo model, used in the transport portion of the simulator that is schematically shown in Fig. 3, is based on the usual Si band-structure for three-dimensional (3-D) electrons in a set of nonparabolic Δ-valleys with energy-dependent effective masses. The six conduction band valleys are included through three pairs: valley pair 1 pointing in the (100) direction, valley pair 2 in the (010) direction, and valley pair 3 in the (001) direction. The explicit inclusion of the longitudinal and transverse masses is important and this is done in the program using the Herring–Vogt transformation [11]. Intravalley scattering is limited to acoustic phonons. For the intervalley scattering, we include both g- and f-phonon processes. It is important to note that, by group symmetry considerations, the zeroth-order low-energy f- and g-phonon processes are forbidden. Nevertheless, three zeroth-order f-phonons and three zeroth-order g-phonons with various energies are usually assumed [12]. We have taken into account this selection rule and have considered two high-energy f- and g-phonons and two low-energy f- and g-phonons. The high-energy phonon scattering processes are included via the usual zeroth-order interaction term, and the two low-energy phonons are treated via a first-order process [13]. The first-order process is not really important for low-energy electrons but gives a significant contribution for high-energy electrons. The low-energy phonons are important in achieving a smooth velocity saturation curve, especially at low temperatures. The phonon energies and coupling constants in our model are determined so that the experimental temperature-dependent mobility and velocity-field characteristics are consistently recovered [14]. At present, impact ionization, Coulomb scattering and surface-roughness scattering are not included in the model. Impact ionization is neglected as, for the drain biases used in the simulation, electron energy [see Fig. 10(a)] is typically insufficient to create an electron-hole pair. Coulomb scattering is of little importance throughout most of the channel, due to low doping, but might yield nontrivial corrections in the implant area. Also, since it is not quite clear how surface roughness scattering behaves in case of carriers displaced from the interface, we believe that any assumption that we might make about it is most likely to obscure the quantum confinement effects (see discussion in Section III).

In solving Poisson's equation, the Monte Carlo simulation is used to obtain charge distribution in the device. We use the Incomplete Lower–Upper decomposition method for the solution of the two-dimensional (2-D) Poisson equation. After solving for the potential, the electric fields are calculated and used in the free-flight portion of the Monte Carlo transport kernel. However, the charges obtained from the EMC simulation are usually distributed within the continuous mesh cell instead of on the discrete grid points. The particle mesh method (PM) is used to perform the switch between the continuum in a cell and discrete grid points at the corners of the cell. The procedures of PM coupling is outlined in the following.

- Assign the charges from within the continuous mesh cell onto the discrete grid points.
- Solve Poisson equation for potentials at those points.
- Calculate electric fields at those points from the potential profiles and obtain the electric fields for particles within the cell.

The charge assignment to each mesh-point depends on the particular scheme that is used. A proper scheme must ensure proper coupling between the charged particles and the Coulomb forces acting on the particles. Therefore, the charge assignment scheme must maintain zero self-forces and a good spatial accuracy of the forces. To achieve this, two major methods have been implemented in the present version of the code: the nearest-grid-point (NGP) scheme and the cloud-in-cell (CIC) scheme. The CIC produces a smoother force interpolation, but introduces self-forces on nonuniform meshes. These issues have been dealt with extensively by Hockney and Eastwood [15], and quite recently by Laux [16].

The device current is determined by using two different, but consistent methods. First, by keeping track of the charges entering and exiting each terminal, the net number of charges over a period of the simulation can be used to calculate the terminal current. The method is quite noisy, due to the discrete nature of the electrons. In the second method, the sum of the electron velocities in a portion of the device is used to calculate the current. For this purpose, the device is divided into several sections along the x-axis (along the semiconductor/oxide interface). The number of electrons, and their corresponding velocities, are added up for each section after each free-flight time step. The total x-velocity in each section is then averaged over several time steps to determine the current for that section. The total device current is determined from the average of several sections, which gives a much smoother result than that based on counting the terminal charges. By breaking the device into sections, individual section currents can be compared to verify that the currents are uniform. In addition, sections near the source and drain regions may have a high y-component in their velocity and should be excluded from the current calculations. Finally, by using several sections in the channel, the average energy and velocity of electrons along the channel is checked to ensure proper physical characteristics.

III. Effective Potential Approach

The inclusion of one-particle quantum effects in the description of the inversion layer at the semiconductor/oxide interface of an MOS device involves solving the Schrödinger equation for the carriers in an approximately triangular potential well. As a result, one obtains bound states, which give rise to two major features: reduced sheet density and charge set-back. Namely, since the lowest bound state can be regarded as the new bottom of the conduction band, the spacing between the Fermi level and the conduction band edge is effectively increased, which results in reduced sheet charge density with respect to the case in which quantum effects are excluded. Moreover, the probability density in the lowest bound state now has a maximum away from the semiconductor/oxide interface, resulting in charge displacement from the oxide, and consequently, an effective increase in the oxide thickness.

An alternative to solving the Schrödinger wave equation is the use of quantum potentials. The idea of quantum potentials originates from the hydrodynamic formulation of quantum mechanics, first introduced by de Broglie and Madelung [17]–[19], and later developed by Bohm [20], [21]. In this picture, the wave function is written in complex form in terms of its amplitude $R(\boldsymbol{r}, t)$ (the density function) and phase $\psi(\boldsymbol{r}, t) = R(\boldsymbol{r}, t)\exp[iS(\boldsymbol{r}, t)/\hbar]$. These are then substituted back into the Schrödinger equation to obtain the following coupled equations of motion for the density and phase

$$\frac{\partial \rho(\boldsymbol{r}, t)}{\partial t} + \nabla \cdot \left(\rho(\boldsymbol{r}, t)\, \frac{1}{m}\, \nabla S(\boldsymbol{r}, t) \right) = 0 \tag{1}$$

$$-\frac{\partial S(\boldsymbol{r}, t)}{\partial t} = \frac{1}{2m}\left[\nabla S(\boldsymbol{r}, t)\right]^2 + V(\boldsymbol{r}, t) + Q(\rho, \boldsymbol{r}, t) \tag{2}$$

where $\rho(\boldsymbol{r}, t) = R(\boldsymbol{r}, t)^2$ is the probability density. By identifying the velocity as $\boldsymbol{v} = \nabla S/m$, and the flux as $\boldsymbol{j} = \rho \boldsymbol{v}$, equation (1) becomes the continuity equation. Hence, (1) and (2) arising from this so-called *Madelung transformation* to the Schrödinger equation have the form of classical hydrodynamic equations with the addition of an extra potential, often referred to as the *quantum* or *Bohm potential*, written as

$$Q = -\frac{\hbar^2}{2mR}\nabla^2 R \rightarrow -\frac{\hbar^2}{2m\sqrt{n}}\frac{\partial^2 \sqrt{n}}{\partial x^2} \tag{3}$$

where the density n is related to the probability density as $n(\boldsymbol{r}, t) = N\rho(\boldsymbol{r}, t) = N\sqrt{R(\boldsymbol{r}, t)}$, Nbeing the total number of particles. The Bohm potential essentially represents a field through which the particle interacts with itself. It has been used, for example, in the study of wave packet tunneling through barriers [22], where the effect of the quantum potential is shown to lower or smoothen barriers, and hence "allows" for the particles to leak through.

An alternative form of the quantum potential was proposed by Iafrate, Grubin and Ferry [23], who derived a form of the quantum potential based on moments of the *Wigner–Boltzmann equation*, the kinetic equation describing the time evolution of the Wigner distribution function [24]. Their form, based on moments of the Wigner function in a pure state, and involving an expansion of order $O(\hbar^2)$, is given by

$$V_Q = -\frac{\hbar^2}{8m}\frac{\partial^2(\ln n)}{\partial x^2} \tag{4}$$

which is sometimes referred to as the *Wigner potential* or as the *density gradient correction.*

Later on, Ferry and Zhou derived a form for a smooth quantum potential [25] based on the effective classical partition function of Feynman and Kleinert [26]. More recently, Gardner and Ringhofer [27] derived a smooth quantum potential for hydrodynamic modeling, valid to all orders of $\hbar^2$, which involves a smoothing integration of the classical potential over space and temperature. There it was shown that, close to the equilibrium regime, the influence of the potential on the ensemble can be replaced by the classical influence of a smoothed nonlocal barrier potential. While this effective potential depends nonlocally on the density, it does not directly depend on its derivatives. Through this effective quantum potential, the influence of barriers on an electron is felt at quite some distance from the barrier. The smoothed effective quantum potential has been used successfully in quantum-hydrodynamic simulations of resonant tunneling effects in one-dimensional (1-D) double-barrier structures [28].

In analogy to the smoothed potential representations discussed previously for the quantum hydrodynamic models, it is desirable to define a smooth quantum potential for use in quantum particle-based simulations. Ferry [10] has suggested an *effective potential* that emerges from the wave packet description of particle motion, where the extent of the wave packet spread is obtained from the range of wavevectors in the thermal-distribution function (characterized by an electron temperature). The effective potential, V_{eff}, is related to the

self-consistent Hartree potential, V, obtained from the Poisson equation, through an integral smoothing relation

$$V_{\text{eff}}(\boldsymbol{x}) = \int V(\boldsymbol{x}+\boldsymbol{y})G(\boldsymbol{y},\, a_0)\, d\boldsymbol{y} \tag{5}$$

where G is a Gaussian with the standard deviation a_0. As shown schematically in Fig. 3, V_{eff} is then used to calculate the electric field that accelerates the carriers in the transport kernel of the simulator described in Section II. This is the approach used in the present simulation, and it actually reduces the infamous noise characteristic for particle-based simulator, due to the integral relation between V and V_{eff} (5). Other quantum potentials, depending on derivatives of the density, may amplify the noise, and are best suited for hydrodynamic simulators. For an example of incorporating quantum potentials in Monte Carlo simulators, see [29].

There is a mathematical connection between this effective potential and the quantum potential, which can be demonstrated by using a Taylor series expansion. For simplicity, we show this in one dimension; similar results apply in higher-dimensional systems. Expanding (5) in a Taylor series in one dimension yields

$$\begin{aligned} V_{\text{eff}}(x) &= \frac{1}{\sqrt{2\pi}\, a_0} \int_{-\infty}^{\infty} V(x+\xi) e^{-\xi^2/2a_0^2}\, d\xi \\ &\cong \frac{1}{\sqrt{2\pi}\, a_0} \int_{-\infty}^{\infty} \left[V(x) + \xi \frac{\partial V}{\partial x} + \frac{\xi^2}{2} \frac{\partial^2 V}{\partial x^2} + \cdots \right] \\ &\quad \cdot e^{-\xi^2/2a_0^2}\, d\xi. \end{aligned} \tag{6}$$

The second term cancels due to the symmetry of the Gaussian, so the third term becomes the leading correction. Thus

$$V_{\text{eff}}(x) = V(x) + a_0^2 \frac{\partial^2 V}{\partial x^2} + \cdots. \tag{7}$$

In nondegenerate semiconductors, the dependence of the density upon the potential is typically proportional to $\exp(-\beta V)$. Using this, we can substitute for the potential in (7), which yields

$$\begin{aligned} V_{\text{eff}}(x) &= V(x) - \frac{2a_0^2}{\beta} \frac{\partial^2 \ln\left(\sqrt{n/n_0}\right)}{\partial x^2} + \cdots \\ &= V(x) - \frac{2a_0^2}{\beta\sqrt{n}} \frac{\partial^2 \sqrt{n}}{\partial x^2} + \cdots. \end{aligned} \tag{8}$$

Within a factor of two, the second term is now recognized as the density gradient term, but is more commonly known as the Bohm potential discussed earlier.

When implementing the effective potential approach due to Ferry [10], one of the questions that one would naturally ask is related to the actual value of the Gaussian smoothing parameter a_0. Also, there has been a debate as to whether the smoothing parameter will depend upon the shape of the confining potential or the substrate doping density. For this purpose, we first apply the effective potential approach to a simple MOS capacitor structure in which the band-bending leads to triangular confinement. The oxide thickness of the MOS capacitors being simulated is 6 nm, and the substrate doping density equals 10^{17} and 10^{18} cm^{-3}, respectively. The results of these simulations are shown in Fig. 4(a) and (b), where we show the gate-voltage dependence of the inversion charge density, and the average distance of the carriers from the interface [30]. From the results shown in Fig. 4, it is obvious that the use of a single Gaussian smoothing parameter $a_0 = 0.5$ nm along the growth direction, can quite accurately describe the reduction in the inversion layer electron density due to quantum-mechanical space-quantization effect. It also leads to accurate description of the displacement of the carriers away from the semiconductor–oxide interface, which, in turn, gives rise to the quantum capacitance, in series with the oxide capacitance.

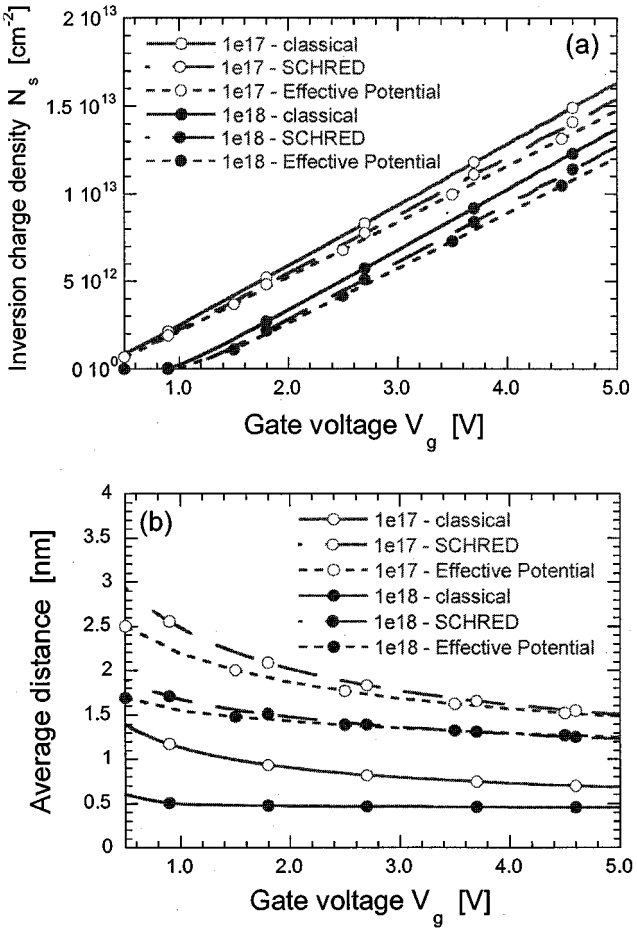

Fig. 4. (a) Sheet electron density and (b) average displacement of the carriers from the semiconductor/oxide interface as a function of the gate voltage. For each doping density, we use classical charge description, fully quantum-mechanical charge description via SCHRED, and Gaussian smoothing of the Hartree potential (the effective potential approach).

The use of V_{eff} has a fairly low nominal computational cost (less than 10% increase in CPU time). However, the size of the smoothing parameter a_0 sets an upper limit on the mesh size, which leads to problems with undesirably many gridpoints in large devices, such as that considered in this paper. Restricting the application of V_{eff} to an area near the interface, where quantum confinement is important, and ignoring it elsewhere, somewhat alleviates this computational burden. However, it introduces a small artificial electric field at the boundaries of this area, which disrupts reaching self-consistency and is the main reason for the overall increase in computation time.

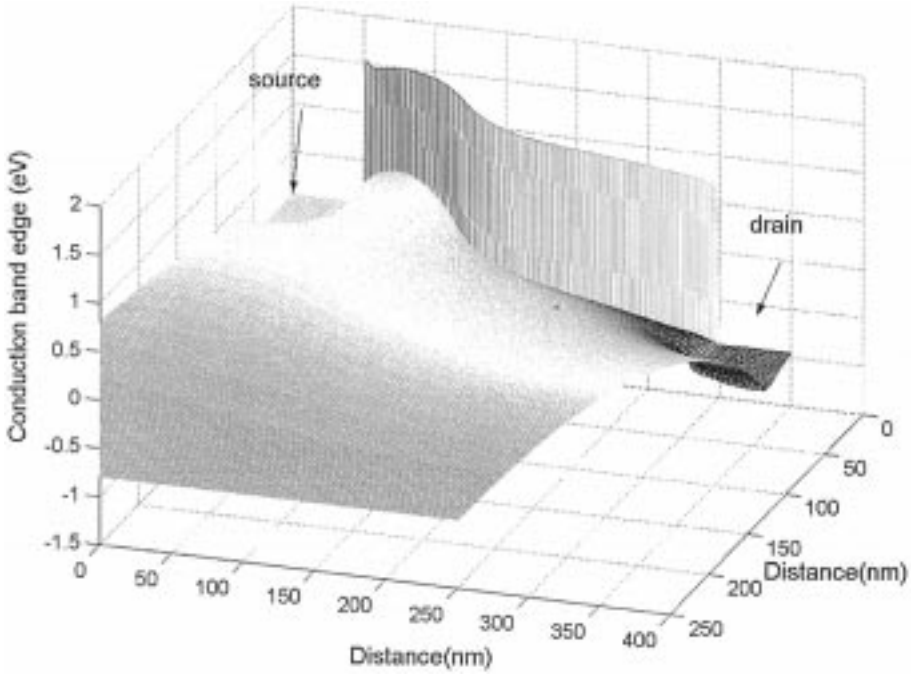

Fig. 5. Conduction band edge for the case when $V_{\rm eff}$ calculation is included in the model. We use $V_G = V_D = 1$ V in these simulations.

IV. Results and Discussion

A schematic of the 250 nm FIBMOS device we simulate is shown in Fig. 2. The substrate doping equals 10^{16} cm^{-3}, source/drain doping is 10^{19} cm^{-3}, junction depth is 36 nm, and bulk depth equals 400 nm. The oxide thickness is 5 nm and the width of the device being simulated is 1.4 μm. The width of the FIB region is 70 nm, the depth equals the junction depth, and the doping density is 1.6 $\times 10^{18}$ cm^{-3}.

In Fig. 5, we show the conduction band edge, found in the device simulation, for the bias conditions $V_G = V_D = 1$ V. From the result shown, one can see that the effective potential shifts the conduction band edge upwards. It, therefore, accounts for the so-called band-gap widening effect due to the quantum mechanical space-quantization in the triangular potential well near the Si–SiO_2 interface. This upward shift of the conduction band edge leads to a reduction of the carrier density at the interface proper. Also, the electrons are moved away from the interface because of the additional perpendicular electric field in the vicinity of the Si–SiO_2 interface. This latter observation is more clearly seen in the results shown in Figs. 6 and 7, where we plot the electron density at the source end of the channel and the average displacement of the carriers from the semiconductor/oxide interface for the bias conditions from Fig. 5. For example, for the case when we include $V_{\rm eff}$ in the model, there is a spread of about 5 nm of the channel electron density in the vicinity of the p^+-implant [Fig. 6(a)]. On the other hand, when $V_{\rm eff}$ is omitted from the model, the electron density spread in the vicinity of the p^+-implant reduces to ~2–3 nm [Fig. 6(b)], which suggests stronger confinement of the carriers at the interface. As shown in Fig. 7, the upward shift of the conduction band edge leads to approximately half an order of magnitude decrease in the sheet electron density, which is consistent with the quantum-mechanical simulations.

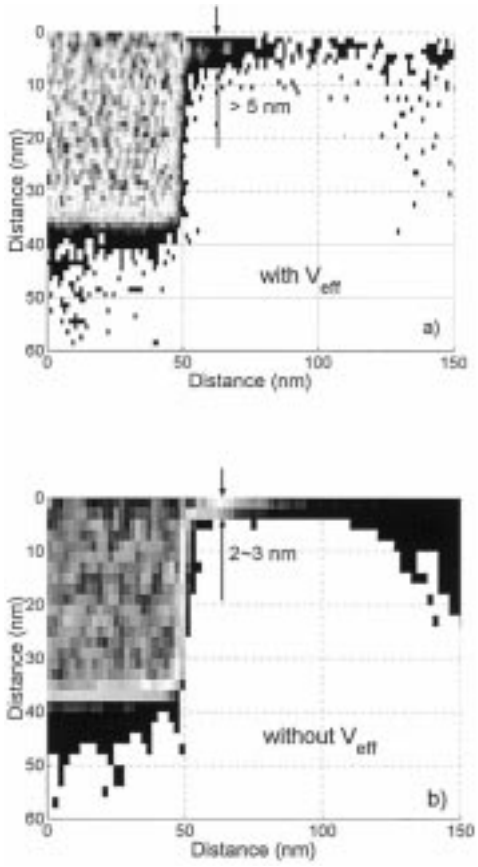

Fig. 6. Electron density near the source end of the channel for $V_D = V_G = 1.0$ V. Top panel corresponds to the case when $V_{\rm eff}$ is included in the model and bottom corresponds to the case without $V_{\rm eff}$.

The quantization of charge in the inversion layer produces an expected increase of the threshold voltage in the channel. This

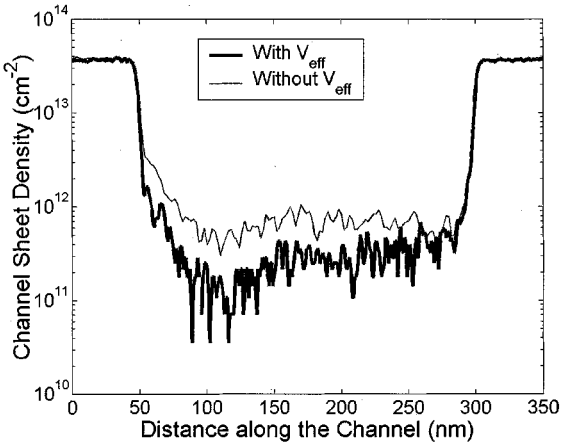

Fig. 7. Sheet carrier density for $V_D = V_G = 1.0$ V, with and without V_{eff}.

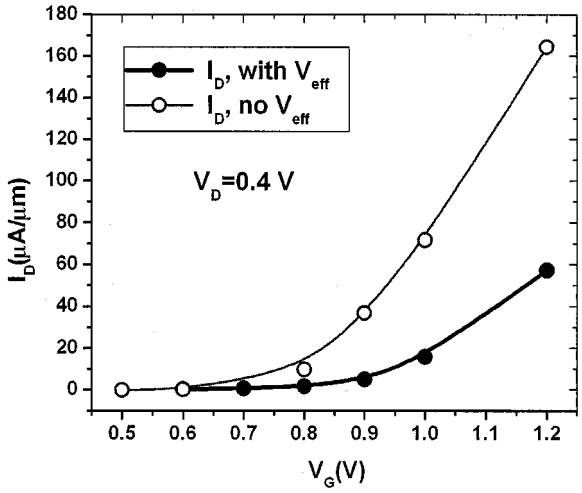

Fig. 8. Device transfer characteristics for $V_D = 0.4$ V.

observation is more clearly seen from the results shown in Fig. 8, where we plot the linear drain current I_D as a function of the gate voltage V_G, for a drain voltage of $V_D = 0.4$ V. If we take as a criterion for determining the threshold voltage as being the gate voltage for which the drain current equals 10 μA/μm, we obtain a shift of approximately 200 mV when space-quantization effects are included in the model. This result, taking into account the very high doping density of the p^+-implant, is consistent with some previous observations [31].

The device output characteristics are shown in Fig. 9 for V_G equal to 1.0 V and 1.2 V, with and without V_{eff}. There are three noteworthy features in this figure: with V_{eff}, the drive current is reduced, the threshold voltage (V_{th}) is increased, and the transconductance is degraded. The inclusion of V_{eff} reduces the drain current I_D, due to two factors: the reduced average carrier velocity and the reduced sheet density, the latter being predominant. Also, since the slope of the I_D–V_D curve in the linear region is proportional to V_G–V_{th}, we see that for a given V_G the inclusion of V_{eff} increases V_{th}, in agreement with the reduction in sheet density, as presented in Fig. 7. Finally, if for a given V_D we analyze the current increase between V_G equal to 1.0 V and 1.2 V, which is (roughly) proportional to transconductance,

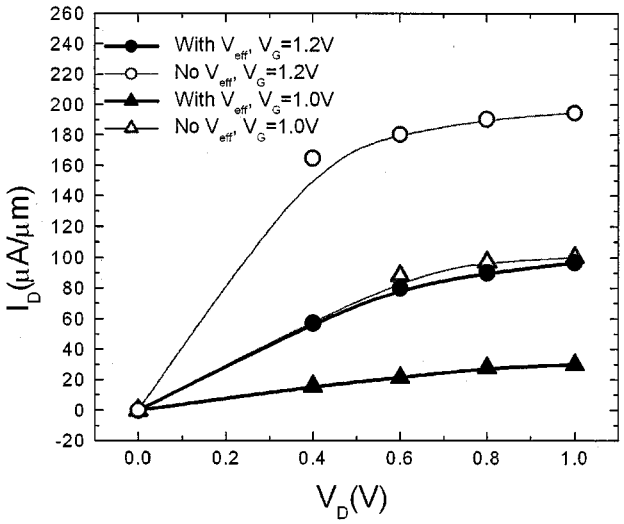

Fig. 9. Device output characteristics for $V_G = 1.0$ and $V_G = 1.2$ V.

it is clear that transconductance is lower with V_{eff} included, as expected according to the charge set-back depicted in Fig. 6.

In Fig. 10(a), we show the average carrier energy of the carriers along the channel. The energy is calculated with respect to the conduction band edge defined by the self-consistent Hartree potential V. Therefore, if the effective potential is included, an increase of the average electron energy of approximately 100 to 150 meV is observed, which corresponds to the upward shift of the conduction band edge defined by V_{eff} with respect to that defined by V. Also, we find that the average carrier energy peaks at the p^+-implant region where the high doping density leads to very large electric fields. At the drain end of the channel, low in-plane fields and significant phonon scattering give rise to a reduction of the average electron energy. These trends are observable regardless of whether we included or omitted the effective potential in the theoretical model.

We observe the same trends in the average carrier velocity, shown in Fig. 10(b), as for the average electron energy. Namely, the velocity overshoot effect is quite evident in the right portion of the p^+-implant region due to the large in-plane electric fields that give rise to fast acceleration of the carriers. Once the carriers enter the low-field region (the middle and the drain end of the channel), the average electron velocity initially decreases and then exhibits a very slight increase. Also noticeable is the fact that the inclusion of V_{eff} does not influence the magnitude of the velocity overshoot but has significant influence on the velocity at the drain-end of the channel. There, a reduction in the velocity is observed because of the in-plane electric field reduction due to the lateral smearing of the potential energy profile. The above effects are consistent with the drain current reduction discussed in conjunction with Fig. 9.

The features in Fig. 10 indicate that the interplay of the asymmetry and quantum effects gives rise to novel transport features. Namely, the band-gap widening and charge set-back, analyzed earlier, are essentially equilibrium quantum features, as their magnitude is virtually the same for either zero or nonzero drain bias. However, it has been shown [32] by carefully achieving the same inversion conditions with and without the effective potential (equal sheet charge density, perpendicular electric field) and

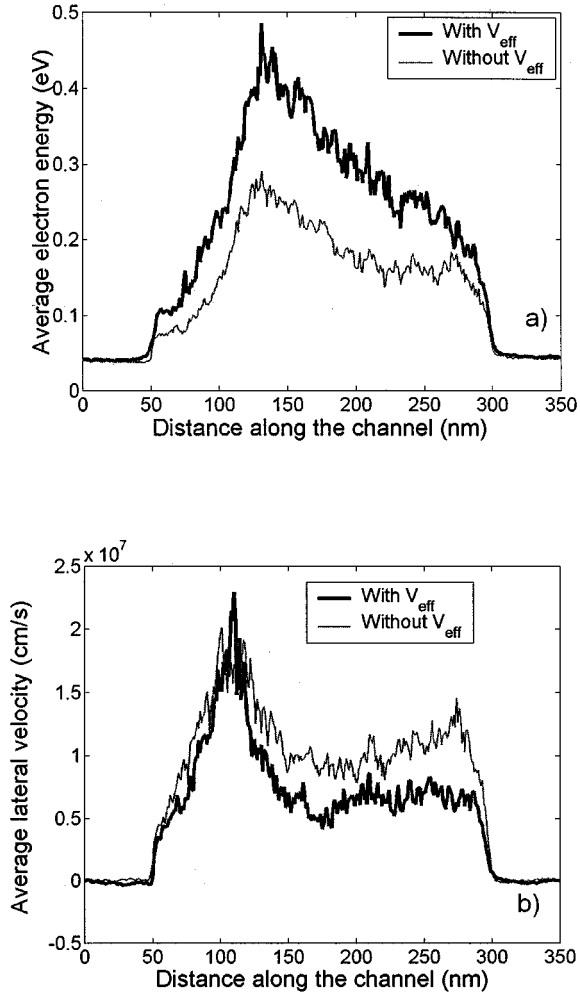

Fig. 10. (a) Average electron energy and (b) average electron velocity for $V_G = V_D = 1.0$ V.

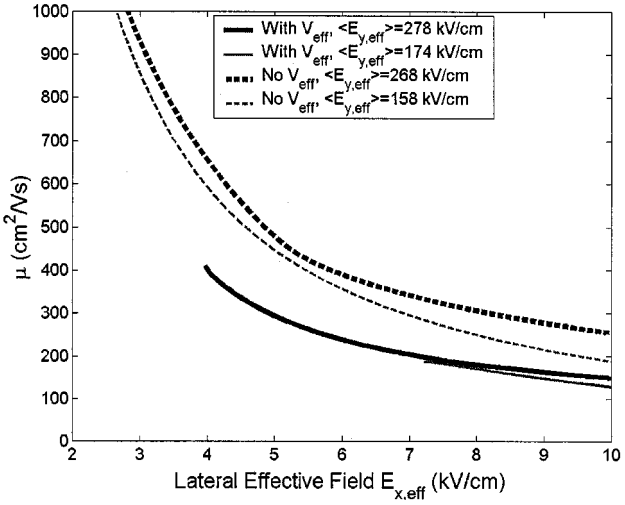

Fig. 11. Variation of low-field mobility with the lateral effective field, with and without $V_{\rm eff}$, for several perpendicular electric fields.

thereby virtually eliminating the differences due to the equilibrium effects of quantization, that quantum-mechanical lowering of low-field mobility exists, which is a purely nonequilibrium effect. In Fig. 11, low-field mobility as a function of the applied drain bias is shown, with and without the effective potential, for different values of the perpendicular electric field. It is noteworthy that asymmetry of the device leads to ballistic features, as already seen in Fig. 10; however, these tend to be suppressed by the inclusion of quantum effects [32]. This implies that highly asymmetric devices may seem faster according to classical estimates, but proper inclusion of quantum effects in the mobility modeling will decide whether transport indeed is ballistic.

V. Conclusions

We employed an effective potential approach to take into account quantum-mechanical effects in a 250 nm FIBMOS device. We find that the quantum-mechanical space-quantization effect leads to a sheet charge density reduction and average displacement of carriers from the interface. This in turn affects the threshold voltage. We find a threshold voltage shift of about 200 mV when the effective potential is included in the model. The increase in the threshold voltage gives rise to the on-state current reduction of 30 to 40%, depending upon the gate voltage bias. Larger degradation is observed for larger gate voltage V_G. Also, an increase in the average electron energy is observed, which is consistent with the decrease in the average drift velocity at the drain end of the channel. This latter observation is in agreement with the drastic reduction in the drain current and with the transconductance degradation, which are results of quantum-mechanically-induced degradation of the equivalent oxide capacitance (due to charge set-back) and of the low-field mobility.

Acknowledgment

The authors would like to thank S. M. Goodnick, R. Akis, and D. K. Schroder for valuable discussions during the preparation of this manuscript.

References

[1] T. N. Buti, S. Ogura, N. Rovedo, and K. Tobimatsu, "A new assymetrical halo source GOLD drain (HS-GOLD) deep sub-half-mictrometer n-MOSFET design for reliability and performance," *IEEE Trans. Electron Devices*, vol. 38, pp. 1757–1764, Aug. 1991.

[2] J. Ma, H.-B. Liang, R. A. Pryor, S. Cheng, M. H. Kaneshiro, C. S. Kyono, and K. Papworth, "Graded-channel MOSFET (GCMOSFET) for high performance, low voltage DSP applications," *IEEE Trans. VLSI Syst.*, vol. 5, pp. 352–359, Apr. 1997.

[3] D. Vignaud, S. Etchin, K. S. Liao, C. R. Musil, D. A. Antoniadis, and J. Melngailis, "Lateral straggle of focused-ion-beam implanted Be in GaAs," *Appl. Phys. Lett.*, vol. 60, no. 18, pp. 2267–2269, 1992.

[4] C.-C. Shen, J. Murguia, N. Goldsman, M. Peckerar, J. Melngailis, and D. A. Antoniadis, "Use of focused-ion-beam and modeling to optimize submicron MOSFET characteristics," *IEEE Trans. Electron Devices*, vol. 45, pp. 453–459, Feb. 1998.

[5] J. Kang, D. K. Schroder, and D. P. Pivin, Jr., "Optimization of FIBMOS through 2-D device simulations," in *Tech. Proc. 3rd Int. Conf. Modeling and Simulation of Microsystems* Boston, MA, 2000, pp. 356–359.

[6] M. Stockinger, A. Wild, and S. Selberherr, "Drive performance of an asymmetric MOSFET structure: The peak device," *Microelectron. J.*, vol. 30, pp. 229–233, 1999.

[7] A. Hiroki, S. Odanaka, and A. Hori, "A high performance 0.1 μm MOSFET with asymmetric channel profile," in *IEDM Tech. Dig.*, 1995, pp. 439–442.

[8] S. Odanaka and A. Hiroki, "Potential design and transport property of 0.1 μm MOSFET with asymmetric channel profile," *IEEE Trans. Electron Devices*, vol. 44, pp. 595–600, Apr. 1997.

[9] J. Kang, X. He, D. Vasileska, and D. K. Schroder, "Optimization of FIBMOS through 2D Silvaco Atlas and 2D Monte Carlo particle-based device simulation," *VLSI Design*, vol. 13, pp. 251–256, 2001.
[10] D. K. Ferry, "The onset of quantization in ultra-submicron semiconductor devices," *Superlatt. Microstruct.*, vol. 27, pp. 61–66, 2000.
[11] C. Herring and E. Vogt, "Transport and deformation-potential theory for many-valley semiconductors with anisotropic scattering," *Phys. Rev.*, vol. 101, pp. 944–961, 1956.
[12] C. Jacoboni and L. Reggiani, "The Monte Carlo method for the solution of charge transport in semiconductors with applications to covalent materials," *Rev. Mod. Phys.*, vol. 55, pp. 645–705, 1983.
[13] D. K. Ferry, "First-order optical and intervalley scattering in semiconductors," *Phys. Rev. B*, vol. 14, pp. 1605–1609, 1976.
[14] W. J. Gross, D. Vasileska, and D. K. Ferry, "3-D Simulations of ultrasmall MOSFET's with real-space treatment of the electron–electron and electron–ion interactions," *VLSI Design*, vol. 10, pp. 437–452, 2000.
[15] R. W. Hockney and J. W. Eastwood, *Computer Simulation Using Particles*. Maidenhead, U.K.: McGraw-Hill, 1981.
[16] S. E. Laux, "On particle-mesh coupling in Monte Carlo semiconductor device simulation," *IEEE Trans. Computer-Aided Design*, vol. 15, pp. 1266–1277, 1996.
[17] L. de Broglie, "Sur la possibilité de relier les phénomènes d'interference et de diffraction á la théorie des quanta de luminère," in *C. R. Acad. Sci.*, vol. 183, Paris, 1926, pp. 447–448.
[18] ——, "La structure atomique de la matière et du rayonnement et la Mécanique ondulatoire," in *C. R. Acad. Sci.*, vol. 184, Paris, 1927, pp. 273–274.
[19] E. Madelung, "Quantatheorie in hydrodynamischer form," *Z. Phys.*, vol. 40, pp. 322–326, 1926.
[20] D. Bohm, "A suggested interpretation of the quantum theory in terms of hidden variables. I.," *Phys. Rev.*, vol. 85, pp. 166–179, 1952.
[21] ——, "A suggested interpretation of the quantum theory in terms of hidden variables. II," *Phys. Rev.*, vol. 85, pp. 180–193, 1952.
[22] C. Dewdney and B. J. Hiley, "A quantum potential description of one-dimensional time-dependent scattering from square barriers and square wells," *Found. Phys.*, vol. 12, pp. 27–48, 1982.
[23] G. J. Iafrate, H. L. Grubin, and D. K. Ferry, "Utilization of quantum distribution functions for ultra-submicron device transport," *J. Phys.*, vol. 42, Colloq. 7, pp. 307–312, 1981.
[24] E. Wigner, "On the quantum correction for thermodynamic equilibrium," *Phys. Rev.*, vol. 40, pp. 749–759, 1932.
[25] D. K. Ferry and J.-R. Zhou, "Form of the quantum potential for use in hydrodynamic equations for semiconductor device modeling," *Phys. Rev. B*, vol. 48, pp. 7944–7950, 1993.
[26] P. Feynman and H. Kleinert, "Effective classical partition functions," *Phys. Rev. A*, vol. 34, pp. 5080–5084, 1986.
[27] C. L. Gardner and C. Ringhofer, "Smooth quantum potential for the hydrodynamic model," *Phys. Rev. E*, vol. 53, pp. 157–167, 1996.
[28] C. Ringhofer and C. L. Gardner, "Smooth QHD model simulation of the resonant tunneling diodes," *VLSI Design*, vol. 8, pp. 143–146, 1998.
[29] H. Tsuchiya, B. Fischer, and K. Hess, "A full-band Monte Carlo model for silicon nanoscale devices with a quantum mechanical correction of the potential," in *IEDM Tech. Dig.*, vol. 12-4, 2000.
[30] R. Akis, S. Milicic, D. K. Ferry, and D. Vasileska, "An effective potential method for including quantum effects into the simulation of ultra-short and ultra-narrow channel MOSFETs," in *Proc. 4th Int. Conf. Modeling and Simulation of Microsystems*, Boston, MA, 2001, pp. 550–553.
[31] D. Vasileska and D. K. Ferry, "The influence of space quantization effects on the threshold voltage, inversion layer and total gate capacitance in scaled Si-MOSFETs," in *Tech. Proc. 1st Int. Conf. Modeling and Simulation of Microsystems, Semiconductors, Sensors and Actuators* Boston, MA, 1998, pp. 408–411.
[32] I. Knezevic, D. Vasileska, X. He, D. K. Schroder, and D. K. Ferry, "Low-field mobility and quantum effects in asymmetric silicon-based field-effects devices," *J. Computat. Electron.*, to be published.

Irena Knezevic (S'01) received the B.S. degree in physics from the University of Belgrade, Belgrade, Yugoslavia, in 1995. She is currently pursuing the Ph.D. degree in electrical engineering at the Arizona State University, Tempe.

Her research focuses on semiconductor device simulations, quantum transport in nanostructures, and density matrix formalism in theoretical treatment of nonequlibrium processes.

Ms. Knezevic is a student member of the APS.

Dragica Z. Vasileska (M'97) received the B.S.E.E. and the M.S.E.E. degrees from the University Cyril and Methodius, Skopje, Republic of Macedonia, in 1985 and 1992, respectively, and the Ph.D. degree from Arizona State University (ASU), Tempe, in 1995.

From 1995 to 1997, she held a Faculty Research Associate position within the Center of Solid-State Electronics Research at ASU. In the fall of 1997, she joined the Faculty of Electrical Engineering at ASU. Her research interests include semiconductor device physics and semiconductor device modeling with strong emphasis on quantum transport and Monte Carlo particle-based simulations. She has published more than 50 journal publications, over 30 conference proceedings and refereed papers, and has given a number of invited talks.

Dr. Vasileska is a member of APS and is on the program or the organizing committee of several national and international conferences.

David K. Ferry (S'61–M'62–SM'72–F'87) received the B.S.E.E. and M.S.E.E. from Texas Tech University, Lubbock, in 1962 and 1963, respectively, and the Ph.D. degree from the University of Texas, Austin, in 1966.

He then spent an NSF Postdoctoral Fellowship in Vienna, Austria. He served as a Member of Faculty at Texas Tech University from 1967 to 1973, then joined the Office of Naval Research, Washington, DC. From 1977 to 1983, he was with Colorado State University, Fort Collins, then joined Arizona State University (ASU), Tempe, where he has served as Director of the Center for Solid State Electronics Research (1983–1989), Chair of Electrical Engineering (1989–1992), and Associate Dean for Research (1993–1995). His work addresses transport physics and modeling of quantum effects in submicron semiconductor devices and electron beam lithography for ultra-submicron quantum functional devices. He has published more than 600 articles, books, book chapters and conference publications.

Dr. Ferry was selected as one of the first Regents' Professors at ASU in 1998, and received the IEEE Cledo Brunetti Award for advances in nanoelectronics. He is a Fellow of the American Physical Society.